Understanding the formation mechanisms of silicon particles from the thermal disproportionation of hydrogen silsesquioxane

Cynthia Cibaka-Ndaya, Kevin O'Connor, Emmanuel Opeyemi Idowu, Megan A. Parker, Éric Lebraud, Sabrina Lacomme, David Montero, Paula Sanz Camacho, Jonathan G.-C. Veinot, Ioan-Lucian Roiban, et al.

Understanding the formation mechanisms of silicon particles from the thermal disproportionation of hydrogen silsesquioxane

Cynthia Cibaka-Ndaya[*1], Kevin O'Connor[2], Emmanuel Opeyemi Idowu[1], Megan A. Parker[1], Eric Lebraud[1], Sabrina Lacomme[3], David Montero[4], Paula Sanz Camacho[1], Jonathan G.-C. Veinot[2], Ioan-Lucian Roiban*[5], Glenna L. Drisko*[1]*

[1]Univ. Bordeaux, CNRS, Bordeaux INP, ICMCB, UMR 5026, F-33600 Pessac, France

[2]University of Alberta, Department of Chemistry, T6G 2G2 Edmonton, Alberta, Canada

[3] Univ. Bordeaux, CNRS, INSERM, Bordeaux Imaging Center, UAR 3420, F-33600 Pessac, France

[4]Sorbonne Université, CNRS, Fédération de Chimie et Matériaux de Paris-Centre, FR 2482, 75252 Paris, France

[5]Univ. Lyon, INSA Lyon, Université Claude Bernard Lyon 1, CNRS, MATEIS, UMR5510, 69621 Villeurbanne, France

ABSTRACT: Crystalline silicon particles sustaining Mie resonances are readily obtained from the thermal processing of hydrogen silsesquioxane (HSQ). Here, the mechanisms involved in silicon particle formation and growth from HSQ are investigated through real time *in situ* analysis in an environmental transmission electron microscope and X-ray diffractometer. The nucleation of Si nanodomains are observed starting around 1000 °C. For the first time, a highly mobile intermediate phase is experimentally observed, thus demonstrating a previously unknown growth mechanism. At least two growth processes occur simultaneously: the coalescence of small particles into larger particles and a growth mode by particle displacement through the matrix toward the HSQ grain surface. Post-synthetic characterization by scanning electron microscopy further evidences the latter growth mechanism. The gaseous environment employed during synthesis impacts particle formation and growth under both *in situ* and *ex situ* conditions, impacting particle yield and structural homogeneity. Understanding the formation mechanisms of particles provides promising pathways for reducing the energy cost of this synthetic route.

INTRODUCTION

In the development of optical metamaterials with high scattering efficiency, silicon (Si) particles are excellent candidates for meta-atoms, although they should fulfill particular requirements regarding their size, crystallinity and density to support Mie resonances.[1,2] Specifically, for optical applications in the visible, particles should be between 75-200 nm, highly crystalline and non-porous. Applications of resonant Si particles include anti-counterfeit labels[3], nonlinear nanophotonics[4] and enhanced Raman scattering[5,6], among others. Optimizing a bottom-up synthesis method to easily obtain resonant units with the desired characteristics could open

pathways toward large-scale fabrication of highly efficient metamaterials [7,8]. One of the most promising fabrication methods currently available is the thermal disproportionation of silicon-rich oxide compounds, in particular hydrogen silsesquioxane (HSQ), $[HSiO_{3/2}]_n$, producing objects that fully possess the desired criteria for resonant silicon particles.[9–13] The main drawbacks of this synthesis are that the synthesis occurs at very high temperatures, and thus is energy-intensive, and that the particles produced are polydisperse in size, and thus need to undergo a size separation process in order to obtain a monodisperse sample.[12,14,15] Perhaps by understanding the particle formation mechanism, it would be possible either to decrease the polydispersity, or to decrease the energy requirements of this synthetic approach.

Despite a few decades of research in this domain, the formation mechanism of the silicon particles via HSQ disproportionation is still not fully understood, particularly above the Si melting point. Several studies report a decrease in the number of silicon nanocrystals, coupled to an increase in their size with increased annealing temperature, which has been hypothesized to be due to Ostwald ripening.[14,16–19] The dissolution of small crystalline particles to the benefit of larger ones in the solid state is curious. These studies mostly involved post-synthetic analysis using various techniques, for example the use of different modes in electron microscopy coupled with atomic simulations.[17,20] However, particle coalescence would also lead to the same post-synthetic observations. In fact, a theoretical study using a combination of quantum mechanical and Monte Carlo simulations suggested two different growth regimes driven by oxygen atom diffusion in a silicon rich oxide compound.[21] The first one, which the authors claim occurs more frequently, is a coalescence-like phenomenon. Two particles in close proximity are not attracted to each other, but combine into a single particle due to the out-diffusion of oxygen in the interspace between them. The second growth regime is a pseudo-ripening process in which the small particles do not dissolve

but instead re-oxidize, thus transferring Si species back into the silicon oxide matrix, which will then be available for the growth of larger particles. Experimental observations of the high temperature process are needed to validate the simulations.

The present work aims to unveil the mechanism of particle formation by investigating the nucleation and growth processes of Si particles from the thermal disproportionation of HSQ, while examining the role of inert versus reducing atmosphere on particle formation. The clear establishment of the phenomena occurring during the transformation of the initial matter requires advanced characterization techniques such as *in situ* analyses that probe the changes from the initial precursors toward the resulting particles in real time. Particularly, environmental transmission electron microscopy (ETEM) allows direct observations of the matter transformations as it interacts with the environmental medium (gas or liquid phase, heating or cooling conditions). The use of this technique offers an new perspective, as previous studies have mostly proceeded by post-synthetic analysis of *ex situ* prepared materials.[16,22]

Here, the formation of Si particles from HSQ was investigated using ETEM. For the first time, a highly malleable and mobile phase, inducing significant particle growth, has been observed experimentally. Multiple growth processes were found, including particle-particle coalescence, and more surprisingly a displacement of the particles through the matrix leaving traces in their wake due to interfacial chemical reactions. The real time observations were complemented with post-synthetic SEM analysis of large particle samples, supporting the growth mechanisms identified in ETEM. *In situ* XRD measurements up to 1200 °C demonstrated a growth mode at the solid state below the melting point of Si. In addition, an investigation by ^{29}Si MAS NMR spectroscopy revealed that thermally processing HSQ under a reducing atmosphere (H_2) induces

more segregation of Si domains, however, they are less homogeneous than when formed under inert conditions (Ar).

RESULTS AND DISCUSSION

In the bottom-up preparation of Si particles from HSQ, spherical silicon particles result from the thermal decomposition of HSQ at high temperatures (> 1000 °C), which leads to disproportionation into crystalline Si particles embedded in a matrix of silica.[9–11] The size of the resulting silicon particles can be tailored by adjusting the processing temperature.[10,11] In a typical synthesis, the particles are then collected after etching the silica matrix with hydrofluoric acid (HF). In the present work, this last step is not used. Instead, the evolution from HSQ at room temperature to the oxide-embedded Si particles at 1300 °C is studied in depth to explore silicon nucleation and growth processes.

Nucleation of Si particles

The decomposition of HSQ first generates matrix-embedded nuclei, as observed by ETEM in a selected area (Figure 1). Figure 1b displays the early stage of particle formation at 1000 °C, with the presence of very small nuclei of about 1 nm visible in the image. The subsequent heating of the analyzed sample resulted in the growth of the nuclei. At 1200 °C, particles of 7 nm in diameter were obtained as seen in (Figures 1c,d). Under the high temperature and set magnifications, it was difficult to assess the crystallinity of the formed particles. Further high-resolution analyses of this region, upon cooling to room temperature, revealed the presence of crystalline Si domains as shown in Figure 1e-f and S1, with a d-spacing value consistent with

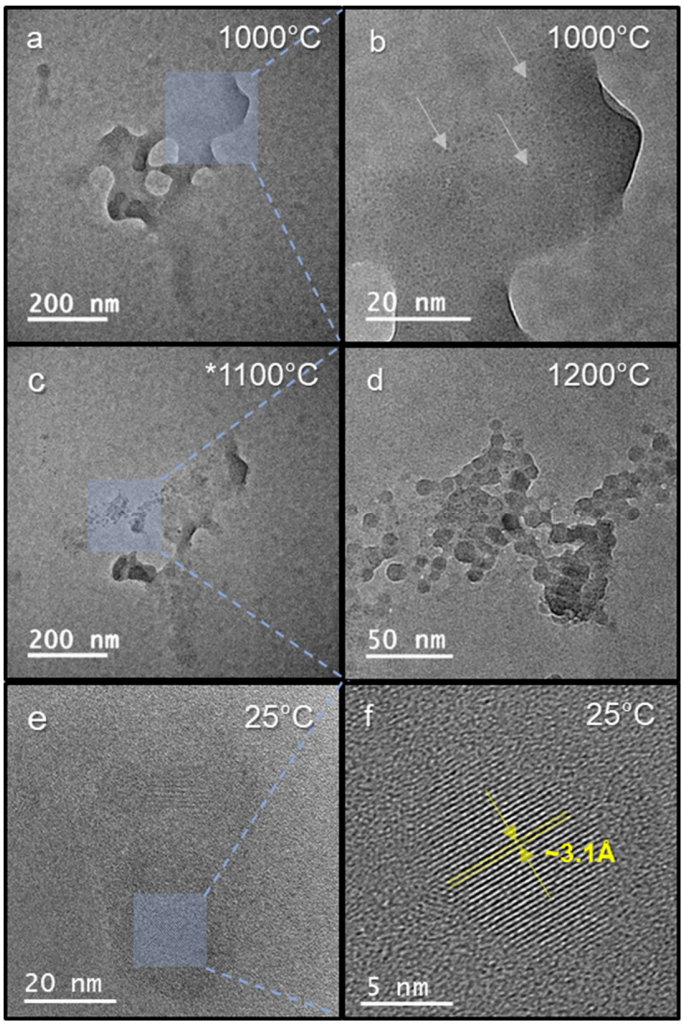

Figure 1. Particle nucleation upon thermal processing of HSQ in a gaseous atmosphere (~20 mbar) of argon. a. An area probed at the early stage of nucleation. b. A higher magnification of a selected region in this area. The higher magnification allows nuclei of about 1 nm to be observed (some are designated by grey arrows). c-d. With temperature increase to 1200 °C, the nuclei evolve to small particles of about 7 nm. (*) The image in c shows the probed area upon cooling to 1100 °C, after growth of particles at 1200 °C for a better comparison. e-f. Images collected in the probed area at room temperature after annealing show the obtained crystalline domains with d-spacing consistent with diamond cubic Si (111) planes.

cubic diamond Si (111) planes. In addition, Figure S1b shows that more nanodomains of crystalline silicon were found in different regions of the sample. These areas were subjected to the same thermal treatment but not illuminated by the electron beam during the process. These observations confirmed that, at this stage, the particle nucleation and growth were essentially originating from the thermal processing of the sample.

These observations were consistent with the general approach reported in previous papers.[16,22,23] These studies concluded that the thermal treatment of silicon rich oxide compounds induces first the segregation and growth of amorphous Si clusters in the approximate temperature range ~400-800 °C. The amorphous Si domains then crystallize around 900 °C and grow. Both the nucleation and the phase transition temperatures from amorphous to crystalline were dependent on the initial composition of the sample of silicon rich oxide. In the present study, the ETEM conditions (pressure around 20 mbar and set magnification) did not allow observation of sub-nanometer silicon domains, if these formed below 1000 °C. Particle nucleation was inhomogeneous throughout the sample. Some regions did not present nuclei, even at the peak temperature of 1300 °C (Figure S2). This is likely due to differences in the local composition of the initial HSQ sample. HSQ was made by a wet-chemistry route (partial hydrolysis & polymerization), so it is possible that the local stoichiometry in any given area of the HSQ could vary, even within the same sample. In addition, HSQ is composed of cage and ladder structures and local variations of the cage: ladder ratio might also impact the resulting nanoparticles.[24] The influence of HSQ inhomogeneity on particle synthesis remains an active area of study. Other areas of the sample showed an abundance of nuclei, which progressively grew in size with increasing temperature.

Particle growth

At the temperatures of 1200 and 1300 °C, the silicon underwent a phase transition to a malleable state with high mobility. At this stage, two different mechanisms were identified for particle growth: the coalescence of particles and growth during displacement through the matrix.

A video provided in supplementary information (Video S1) shows the observed coalescence of particles. Figure 2 presents images retrieved from this video before and after the coalescence occurs. The video shows a decelerated coalescence for better visualization, however the actual video timespan is about 1.2 s and the observed phenomenon occurred in less than one second. The 2 particles, with respective apparent diameters around 8 and 11 nm, displaced simultaneously toward each other, indicating a high mobility of the particles. The combined larger nanoparticle presented a diameter of about 14 nm, albeit non-spherical in shape.

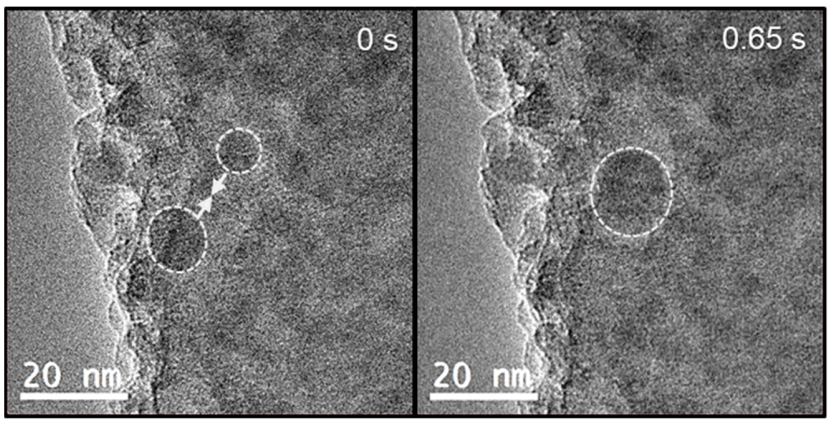

Figure 2. Growth via particle coalescence. Images are collected at the set temperature of 1200 °C in a gaseous atmosphere (~20 mbar) of 95% N_2 and 5% H_2. a. At t=0 s, two particles are well separated. They both displace toward the other particle and coalesce into a single particle.

A second growth mechanism has been observed via particle displacement in the matrix, shown in Video S2 in supplementary information. From this video, three representative images are shown (Figure 3) of a particle moving and changing shape during a 14 s timespan. Here, the morphological changes of the particle throughout the recorded period demonstrate a highly malleable phase: the sphere-like shape evolves into less defined conformations in the way a liquid drop behaves to fill a constrained volume or due to capillary action on a rough surface. A trace is left in the wake of the nanoparticle as it moves through the matrix. This suggests that interfacial chemical reactions occur between the particle surface and the silicon oxide, resulting in adding reduced Si from the matrix to the particle. We assume that oxygen is released during this process. Although the changes are much less pronounced, the same phenomenon takes place in the case of a second particle present in the probed area at the bottom of the images in Figure 3.

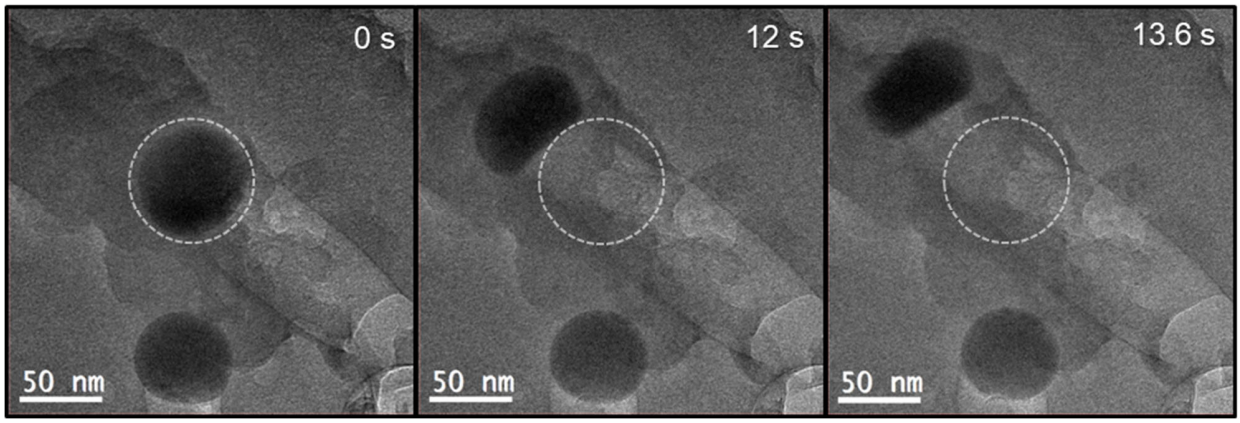

Figure 3. Growth via displacement in the matrix. Images are collected at the set temperature of 1300 °C in a gaseous atmosphere (~20 mbar) of 95% N_2 and 5% H_2. The particle displaces from its initial starting point (indicated by a grey dashed circle) over the course of 14s of observation.

Video S3 and associated Figure 4 clearly summarize the identified growth mechanisms. Black arrows, serving as a guide to the eye in Figure 4a, indicate the coalescence of two particles, with the resulting larger particle seen in Figure 4b. This particle starts to move across the matrix, tracked with the green arrows in Figures 4b-f. Figure 4d shows the particle with a morphological change consistent with a malleable behavior. In addition, in Figures 4d-f, the trace formed upon displacement of the particle within the matrix is observed. The probed area displays a second coalescence event, shown by the black arrows in Figure 4c to Figure 4e. Only a limited number of coalescence events were witnessed in these experiments, however it is reasonable to suppose that this growth mechanism occurs regularly between closely spaced particles with high malleability and mobility. The particles minimize their surface energy upon coalescing into a single particle. One possible explanation of this phenomenon could be the out-diffusion of oxygen in the interspace between closely-spaced particles, as suggested by previously reported Monte Carlo simulations.[21] Moreover, it can be observed that towards the center of the matrix grain imaged here, there is a large particle which is hardly visible in the center of Figure 4a, which becomes progressively more defined by Figure 4f. It appears as though this particle is moving through the matrix, with a displacement in the direction parallel to the electron-beam.

The particles seem to move toward the surface of matrix grains in which they are embedded. During the *in situ* experiments, the particles disappeared very quickly under the electron beam upon reaching the surface and losing the protection from the matrix. Because of this, it was difficult to investigate in real time how they behave upon cooling.

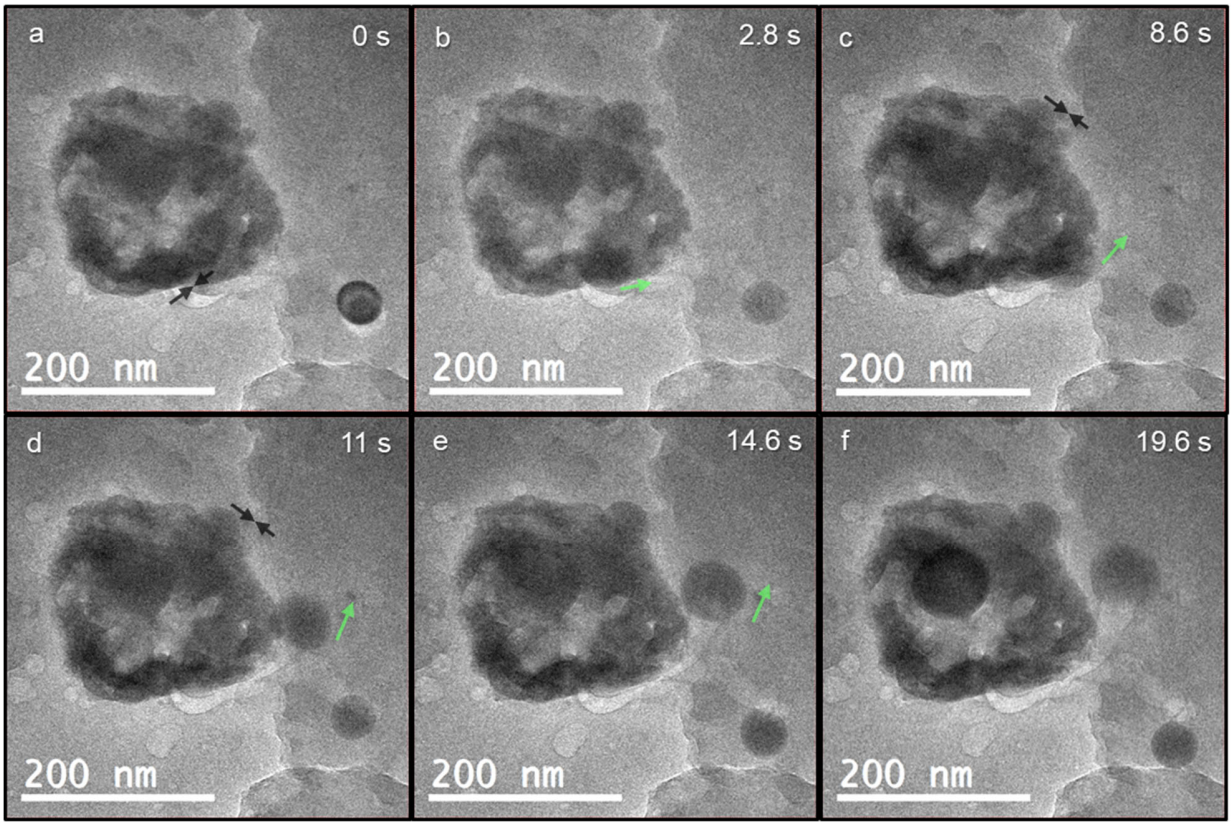

Figure 4. Images summarizing the observed growth modes with particles showing a highly malleable phase. Growth via coalescence and displacement inside the matrix are observed with time, with the video showing a. 0, b. 2.8, c. 8.6, d. 11, e. 14.6 and f. 19.6 s have elapsed since the beginning of the filming. Images are collected at the set temperature of 1300 °C in a gaseous atmosphere (~20 mbar) of 95% N_2 and 5% H_2.

Figure S3 shows that differences are found in the particles obtained by standard *ex situ* annealing and *in situ* heating in the ETEM at 1300 °C. An obvious size discrepancy is observed, with an average diameter of 12 nm for *ex situ* prepared particles, whereas the particles have sizes between ~30 nm to ~100 nm in *in situ* experiments. In addition, ETEM experiments were carried out in either 100% argon or a mixture of 95% nitrogen and 5% hydrogen and Si particles only demonstrated a high mobility and substantial growth when the chamber was filled with a mixture

of N_2 and H_2. The formation of small particles at 1000 °C was achieved independently of the gas used. The most probable explanation for the observation of large particles in ETEM experiments is a fast growth induced by the highly reducing character of the electron beam, coupled with the presence of H_2 at 1300 °C in the microscope chamber. It is however difficult to quantify precisely the extent of the electron beam effect. Several aspects should be taken into account, including the total electron dose sent to the probed area. The synergistic effects enhancing reducing conditions will be the subject of further investigations. Regarding the observed mobility of the growing particles, several aspects might be considered at the temperature of experiments, including the Tamman effect, which induces atomic mobility at a much lower temperature than the melting point. There is melting point depression for nanoscale objects, which might also influence the experiments.

Nonetheless, the growth modes observed for large particles in ETEM seem to be consistent with the growth mechanisms of larger particles under *ex situ* thermal treatment above the melting point of Si (~1410 °C for bulk Si).[14] To support this, post-synthetic analysis of samples were carried out through *ex situ* heating at temperatures higher than the melting point of Si, *i.e.* 1700 and 1500 °C. Figure 4 gives images collected from SEM analysis of these samples, supporting the growth mode by displacement of highly mobile particles toward the surface. Figures 5a,b show the surface of an untreated grain after thermal processing. Particles are observed emerging from the grain surface, which is more easily seen in the magnified image in Figure 4b. This particle is partially emerged from the matrix, with part of the silicon still embedded. Note that Figure 5b reveals a pseudo-spherical shape: facets, formed upon crystallization of the particle when the temperature decreases, characterize the overall sphere-like morphology. An additional example of a particle is provided in Figure S4 to better see these facets. These features are typically not observed after HF etching

in the standard fabrication of Si particles via disproportionation of silicon-rich oxide compounds. Figures 5c-d present internal regions of broken grains from the *ex situ* heated samples. The images are characterized by holes left after the displacement of particles, as well as bumps from particles in the process of moving through the matrix. Traces are visible, where it seems that these tracks are globally oriented in the same direction. This observation suggests that particle displacement may be driven by differences in the density of the silicon particles relative to the matrix (Archimedes' principle). The collected information from SEM analysis supports that the growth mechanisms observed in the ETEM are consistent with what occurs in standard preparations of large Si particles.

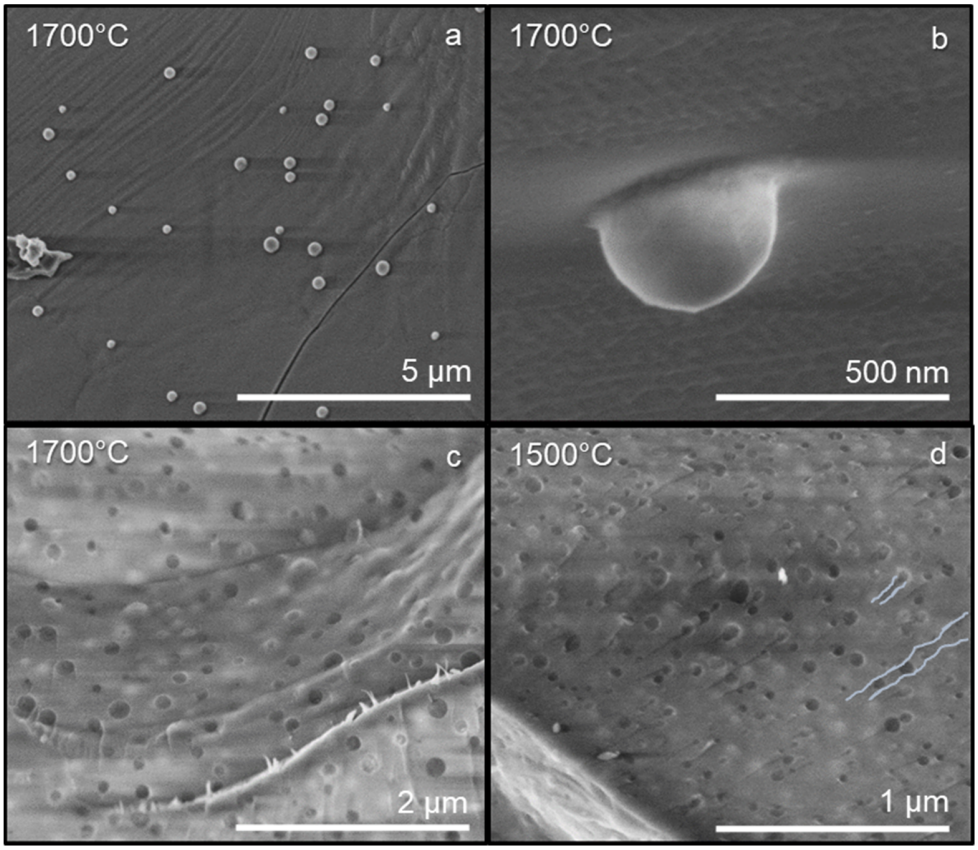

Figure 5. SEM analysis of samples *ex situ* heated to 1700 and 1500 °C under 1 bar of Ar. a. Particles emerging from the surface of a grain; Temp. = 1700 °C. b. Higher magnification of a

selected particle with a view-angle that highlights the particle emerging from the matrix; Temp. = 1700 °C. Inner region of a broken grain: holes, traces and bumps are observed in c. Temp. = 1700 °C and d. Temp. = 1500 °C.

Elemental analysis (STEM – EDX) was performed on the sample *ex situ* heated at 1700 °C in order to confirm the elemental composition of the formed crystalline particles. The results of this analysis are presented in Figures 6a-d. The dark field image in Figure 6a shows the presence of particles, with brighter contrast, within the matrix. A deficit of oxygen is identified at the location of the formed particles (Figure 6b), where there is surplus silicon in these regions (Figure 6c). The overlapping of oxygen and silicon elemental mapping unambiguously shows the silicon particles are surrounded by a silicon oxide matrix (Figure 6d).

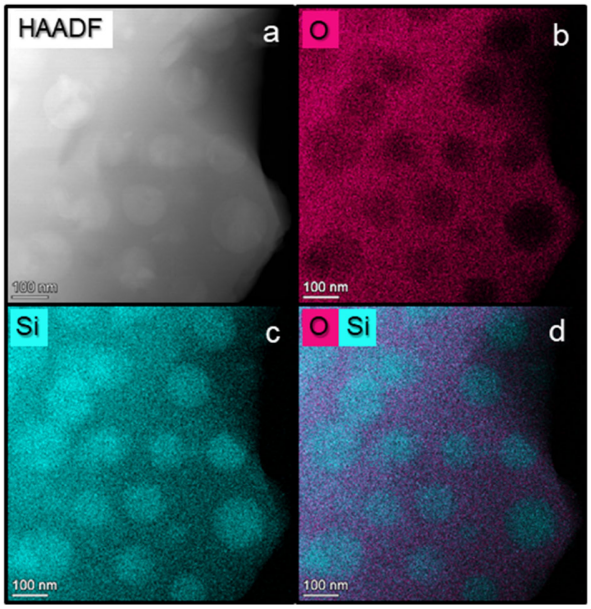

Figure 6. **S**TEM-EDX mapping in high vaccum of a sample *ex situ* heated to 1700 °C under Ar. a. High-angle annular dark-field imaging of the probed region. b. Oxygen mapping. c. Silicon mapping. d. Overlapping mapping of oxygen (in red) and silicon (in blue).

To further explore the real time mechanism without the influence of the electron beam, complementary *in situ* XRD measurements (Figure 7) validated that, below the melting point of Si, a growth route in the solid state takes place. XRD diffractograms were recorded upon thermal annealing of HSQ from room temperature to 1200 °C under nitrogen. The diffractograms displayed in Figure 7b and Figure S5 reveal that approaching 1100 °C, the size of the Si crystallites becomes large enough to induce a diffraction signature. When the temperature is progressively raised to 1200 °C, the intensity of the peaks increases, indicating a greater ratio of crystallites to amorphous content, consistent with crystallization of the nuclei. The sharpness of the peaks increases very slightly, indicating limited particle growth. The crystallinity is conserved during the dwell time of 1 h at 1200 °C, as well as upon sample cooling (Figure S5). Thus, below the melting point of Si, crystallization is progressive, with slow growth. Note that, independently of the temperature, an amorphous phase dominated the XRD patterns due to the presence of the SiO_x matrix surrounding the Si nanocrystals. Moreover, below 400 °C, diffractograms in Figure 7a reveal a broad signal around 10 ° 2θ, which progressively disappears upon increasing temperature up to 400 °C. This feature may relate to the subtle changes in the Fourier transform infrared spectra, reported by C. M. Hessel, *et al.* for *ex situ* processed HSQ below 400 °C.[22] While definitive assignments of these structural changes are yet to be done, the authors suggested HSQ cross-linking and cage rearrangement to be at the origin of the modifications in the initial HSQ FTIR spectrum. The peak at 13° 2θ, present initially, could not be assigned, however it did not show any modifications during the experiment. A peak at 22° 2θ, distinguished at 1200 °C, might be associated to a small fraction of tetragonal SiO_2.

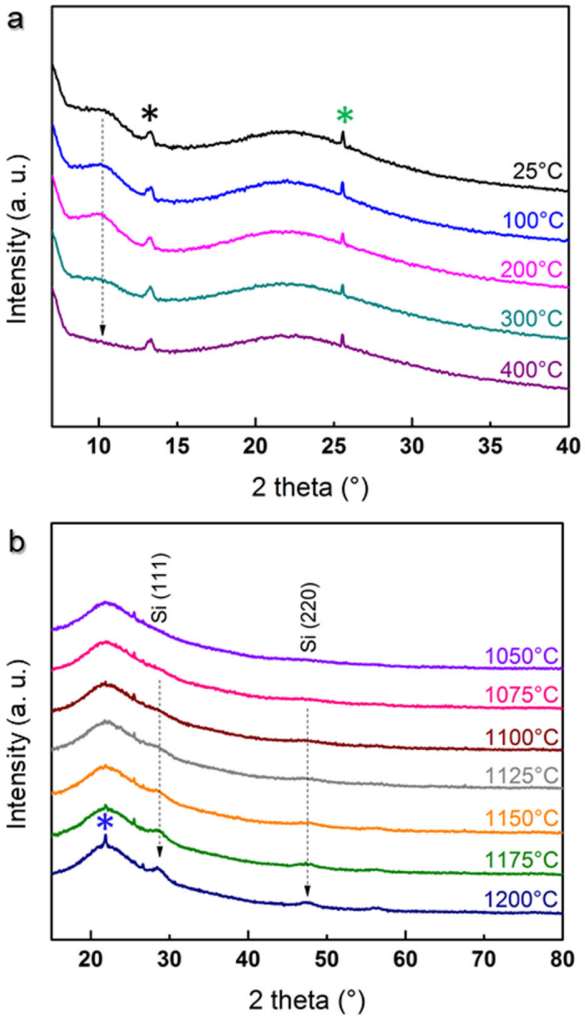

Figure 7. *In situ* powder XRD analysis of HSQ thermal treatment. a. Diffractograms recorded from room temperature to 400 °C highlighting the feature around 10 ° 2Θ. The starred peak at 26 ° 2θ is associated with the alumina sample holder. Black stars at 13° 2θ designate an additional unexpected peak. b. Diffractograms recorded from 1050 to 1200 °C, highlight the progressive appearance of cubic diamond Si signal. The blue star at 22° 2θ designate an additional unexpected peak.

Influence of a reducing atmosphere

In the literature, the preparation of Si particles from thermal processing of silicon-rich oxide compounds are conducted either in a reducing (presence of H_2) or an inert atmosphere. In the

present work, the potential influence of hydrogen in this synthesis route was examined. For this purpose, samples were *ex situ* annealed at three different temperatures (1100, 1200 and 1300 °C) in the presence (95% Ar - 5% H_2) and absence (100% Ar) of hydrogen. Samples were weighed before and after thermal annealing. The weight loss found for all the samples (Table S1) did not present large variation and remained around 5% with only a very slight increase found under the reductive atmosphere compared to inert conditions. The weight loss of 5% is consistent with previously reported thermogravimetric analysis under a 95% N_2 - 5% H_2 mixture[9] and under pure argon.[25] In this later work, the 5% weight loss was attributed to the release of SiH_4 and H_2 species using TGA coupled with mass spectrometry. Here, the obtained oxide-embedded particles were characterized using ^{29}Si MAS NMR spectroscopy, Raman spectroscopy, X-ray diffraction spectroscopy and TEM. Micrographs of the prepared samples are presented in supporting information (Figure S6) and confirm the formation of oxide-embedded nanoparticles. Figure 8 gives the results of the spectroscopic analyses of the samples treated at 1300 °C.

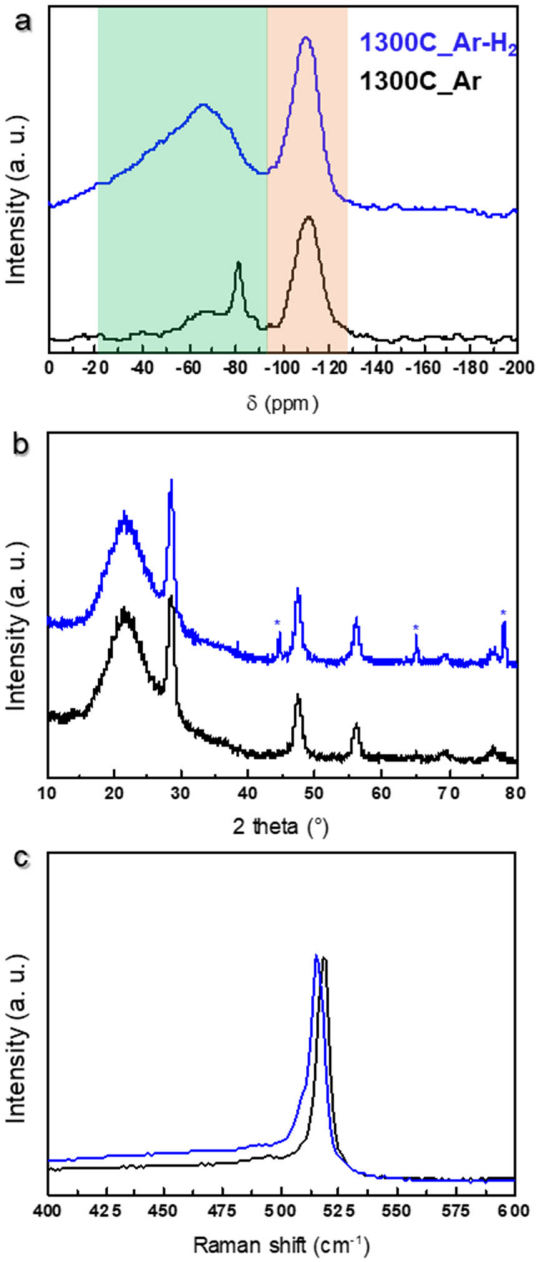

Figure 8. Influence of H_2 presence during particle synthesis. Spectroscopic analyses of samples *ex situ* annealed at 1300 °C under 100% Ar (black) and 95% Ar – 5% H_2 (blue). The spectra are not normalized and the y-axis provides the intensity in arbitrary units. a. Direct excitation ^{29}Si MAS NMR spectra. The spectra are vertically translated for better comparison. b. Powder X-ray diffraction patterns. Stars designate peaks from the aluminum powder XRD holder. c. Representative Raman spectra.

The direct excitation ^{29}Si MAS NMR spectra show different local Si environments for the materials synthesized in a mixed atmosphere of Ar/H_2 compared to pure Ar. Both materials exhibit two well-separated signals coming from the silica matrix (highlighted in orange) and the silicon formed domains (highlighted in green). Provided as a guide, deconvolutions of the spectra are given in Figure S7 in the supporting information. A signal at around -110 ppm is present in both cases, associated with Q_4 species in the SiO_2 matrix. The material synthesized in a pure Ar atmosphere exhibits a very sharp peak (FWHM 4 ppm) at – 81 ppm, previously attributed to c-Si in a highly ordered environment.[26–29] A larger signal around -66 ppm (FWHM 20 ppm) is also found. This latter feature is observed as well in the material synthesized in the presence of hydrogen: a very large Gaussian-like resonance centered at -67 ppm and spanning over -100 ppm. The signal centered at -67 ppm is between the expected responses of elemental silicon in amorphous and crystalline phases (around -40 ppm and -80 ppm respectively).[29,30] Perhaps this resonance originates from a distribution of chemical shifts, as a consequence of local structural disorder or unidentified molecular species. Structural disorder due to strain, structural defects or a large fraction of near-surface sites were previously reported to induce a large range of chemical shifts, as well as a broadening of the responses from amorphous or crystalline silicon.[31] Under reductive synthesis conditions, although not well separated, a contribution of c-Si in a highly ordered environment around -81 ppm cannot be excluded, as this peak spans over -100 ppm. In addition, a signal around -37 ppm is found in the deconvolution of the response of the sample prepared under a reducing atmosphere. This feature could be associated either to amorphous silicon or to $H_2Si(\text{-}SiH_3)\text{-}OSiH_3$ species.[32] Overall, it seems that the presence of hydrogen favors the segregation of Si species (higher percentage associated with elemental Si signal, see Table S2), but the formed silicon nanoparticles are in a more complex environment. In contrast, under inert

conditions, the retrieved percentages of silica were higher and the signal from Si domains suggested a more homogeneous environment. This conclusion supports different chemical reduction pathways when thermally processing HSQ in an inert or reducing atmosphere. The same observations were made for the samples prepared at 1200 and 1100 °C. In addition, and as expected, the formation of Si domains was favored by higher temperature (see Figure S7). Moreover, slight shifts to higher resonance frequency of the peak centered at -67 ppm are observed for the materials synthesized in a mixed atmosphere at 1200 °C and 1100 °C. This might be related to a decrease in particle size from around 12 nm to less than 6 nm (from TEM), as previously observed by A. N. Thiessen, *et al.*[33] This is however, less evident for the material synthesized in pure Ar atmosphere.

Representative patterns obtained from XRD measurements and Raman spectroscopy analysis of samples prepared at 1300 °C are given in Figure 8b,c. In the presence and absence of H_2, the XRD patterns overlap well, though the FWHM in the case of the reducing conditions is slightly narrower (FWHM (2θ) of 0.74° compared to 0.82° in pure Ar), suggesting slightly bigger crystallite size on average (11.6 nm compared to 10.5 nm in pure Ar from Scherrer calculations).

Raman spectroscopy is known to be a very sensitive probe for the local atomic bond order and particle size. The distinct Raman responses are known to be around 520 cm^{-1} for crystalline and 480 cm^{-1} for amorphous bulk silicon.[34–38] In Figure 8c, both samples exhibit Raman responses near the signal expected for crystalline silicon. A very slight redshift (~3 cm^{-1}) is observed for the sample under reducing conditions, but both values remain in the previously reported range for crystalline Si.[35] Redshifts (> 7 cm^{-1}) have previously been attributed to incomplete or incipient crystallization, as well as various sizes of crystallite in the sample,[39] and intermediate range order.[36,40] The work of E. Anastassakis, *et al.* mentioned stresses in the sample at the origin of

slight shifts.[41] For small particles, the average bond energy within a particle decreases, and thus so does the Raman frequency. In the present study, taking into account that the obtained shift at 1300 °C is very small, and was not observed at 1200 °C (Figure S8) and that the XRD patterns seem to favor a slightly higher crystallinity in the case of hydrogen in the medium, it is likely that the crystallinity of both samples does not differ considerably. Possible differences in structural defect density, as observed by NMR spectroscopy, may explain the differences in bond order.

CONCLUSIONS

This study elucidated two mechanisms taking part in the fabrication of Si particles from thermal annealing of HSQ, which may occur in place of, or in addition to, the Ostwald ripening process that has been proposed by others in the field. In particular, ETEM analysis distinguished different growth pathways. For the first time, a highly malleable and mobile silicon phase was observed in real time, which led to substantial particle growth, reaching sizes typically obtained only above the melting point of Si. Growth processes by particle coalescence and particle displacement in the matrix toward the surface were identified. We have thus experimentally validated the theoretical quantum mechanical and Monte Carlo simulations by Yu, et al, showing that coalescence largely contributes to the growth mechanism. SEM analysis of *ex situ* prepared samples of large particles further supported the growth mechanisms identified by *in situ* observations. Most likely, fast particle growth results from the coupling between the reducing character of the electron beam, the presence of H_2 and heat provided a highly reducing environment in ETEM. Therefore, it seems that one way to optimize this synthesis route to reduce energy consumption, while obtaining silicon particle sizes large enough to support Mie resonance, is to provide a highly reducing environment during the reaction.

In addition to the ETEM investigations, *in situ* XRD measurements indicate that crystalline Si domains grew slowly in the solid state below the melting point. This study was complemented by an investigation of the role of a reducing atmosphere in the disproportionation reaction. In particular, ^{29}Si MAS NMR spectroscopy results underlined that different chemical pathways might occur in the presence or absence of hydrogen. A reducing atmosphere seems to induce the formation of more Si domains, however, they are less homogeneous.

Experimental Section

Materials. Toluene (HPLC grade), fuming sulfuric acid (reagent grade, 20% free SO_3 bases), and trichlorosilane (99%) were purchased from MilliporeSigma. Sulfuric acid (reagent grade, 95−98%) was purchased from Fisher Scientific. Dry toluene was dispensed from a Pure-Solv purification system with N_2 operating gas; other reagents were used as received.

Preparation of Hydrogen Silsesquioxane

HSQ was synthesized using an adapted literature procedure.[33] On an Ar-charged Schlenk line, concentrated sulfuric acid (15 mL) and fuming sulfuric acid (7 mL) are mixed in a purged, 2 L, 3-neck round bottom flask. Dry toluene (45 mL) is added dropwise with stirring, followed by a dropwise addition of trichlorosilane (16 mL) in dry toluene (110 mL) overnight. Both additions occur under flowing Ar. The mixture is then decanted into a separatory funnel, isolating the organic layer, and washed three times with a solution of aqueous sulfuric acid (1.2 L H_2O, 0.4 L H_2SO_4). The washed organic layer is dried and neutralized over $MgSO_4$ and $CaCO_3$ overnight. Following gravity filtration, the toluene is removed via rotary evaporation followed by a final evaporation in vacuum, yielding a white solid.

***In situ* investigations.**

ETEM experiments. *In situ* TEM experiments were performed using a FEI ETEM Titan 80-300 microscope operating at 300 kV equipped with a OneView camera from Gatan. As received HSQ grains were ground and dispersed in 2-propanol. Drops of the highly dilute dispersion were deposited on a Si_3N_4 window chip purchased from DENS solutions, compatible with the Wildfire sample holder. The solvent evaporated under air prior to analysis. During experiments, the microscope chamber was filled with a flow of gas at a pressure around 20 mbar. Experiments were performed under pure argon or under a mixture of N_2 - H_2 (95%-5%). In a typical experiment, the temperature was raised from room temperature to 800 °C at a rate of 10 °C/s with ~2 min of plateau every 100 °C. TEM images were not systematically collected in this temperature range. From 850 to 1300 °C, the temperature was increased by step of 50 °C, at a rate of 10 °C/s with plateaus of about 20 min – 1 h at 900, 1000, 1100, 1200 and 1300 °C in order to collect images and record videos. Note that the chips used are certified for sustaining temperatures up to 1100 °C, however a progressive slight increase of the temperature allowed 1300 °C to be reached without damaging the chip. Cooling the sample to room temperature was carried out by step sizes of 100 °C at a rate of -10 °C/s.

In situ XRD. *In situ* X-ray diffractograms in the range 4 – 100° 2θ were collected using a PANalytical X'Pert Pro apparatus (*Co radiation) equipped with an Anton Paar HTK1200 high temperature chamber. XRD measurements were carried out under a flow of nitrogen upon heating and cooling in the range 25 - 1200 °C. The temperature profile was set as followed: from 25 to 100 °C, the temperature was increased at a rate of 60 °C/min. From 100 to 900 °C, a rate of 2 °C/min was applied and sample XRD responses were collected every 100 °C corresponding to a 30 min dwell time. From 900 to 1200 °C, diffractograms were collected every 25 °C. A dwell time

of 1 h was set at 1200 °C before cooling the sample at a rate of -2 °C/min with signals collected every 25 °C until reaching 1000 °C and then every 100 ° C until 100 °C. From 100 °C to 25 °C a decrease rate of 5 °C/min was used.

(*) Cobalt radiation was used during *in situ* XRD measurements and the collected diffractograms were afterward converted to signals from Co to Cu (Kα) wavelength using the software PowDLL Converter.

***Ex situ* investigations.**

Samples preparation. *Ex situ* annealing of HSQ samples were performed in an oven under a constant gas flow rate at atmospheric pressure. HSQ powder was disposed in a crucible and introduced in the oven. For target temperatures of 1100, 1200 and 1300 °C, alumina crucibles were employed. The temperature was raised at a rate of 10 °C/min and a dwell time of 1 h was applied at the peak temperature before cooling to room temperature. For each temperature, syntheses were carried out in two different gaseous conditions: in 100% Ar and in a mixture of Ar-H_2 (95%-5%). In both cases, the gas flow rate was set to 1 mL/s. For target temperatures of 1500 and 1700 °C, yttria - stabilized zirconia crucibles were employed, and syntheses were carried out in pure Ar (5 mL/s). The temperature was raised at a rate of 5 °C/min and a dwell time of 1 h was applied at the peak temperature before cooling to room temperature.

SEM analysis. A field emission gun- scanning electron microscope Hitachi SU-70 was used to perform SEM analysis on samples *ex situ* annealed at 1500 and 1700 °C. Untreated grains as well as broken grains were deposited on carbon tape on SEM sample holders. The samples were not sputter coated and images were collected at a current voltage of 3kV using SE (secondary electron) mode.

TEM analysis. TEM imaging of *ex situ* annealed samples was performed using a Jeol JEM-1400+ apparatus. The thermally processed powders were ground and dispersed in ethanol. Drops of the dispersion were deposited on a carbon film-coated copper TEM grid and ethanol was allowed to evaporate under ambient conditions before analysis**.** ***TEM-EDX.*** For elemental mapping of the oxide-embedded silicon particles, a ThermoFisher (FEI) Talos F200S G2 apparatus operating at 200 kV was used. Images were acquired using the software VELOX (Version 2.13.1.1138-af4e0daa7d).

XRD measurements. X-ray diffractograms from 8 to 80° 2θ were recorded on ground powders using a PANalytical X'Pert Pro apparatus (Cu radiation) equipped with an X'Celerator detector.

Solid-State NMR spectroscopy. Solid-state NMR spectra were recorded using Bruker Avance III spectrometers equipped with either 7.05, or 11.7 T wide-bore superconducting magnets corresponding to the ^{29}Si Larmor frequency of 59.6 MHz and 99.3 MHz, respectively. All data were acquired using a 4 mm double-resonance Bruker MAS NMR probes, with MAS rate of 10 KHz. Chemical shifts were referenced relative to silicon oil at -22 ppm, used as a secondary reference.

Direct excitation ^{29}Si MAS experiments were acquired using a short pulse length of 3-4 μs corresponding to a selective π/2 pulse determined by silicon oil and a recycle interval of 60-400 s.

Although T_1 was very long for all ^{29}Si resonances, there was little difference in the relative relaxation rates, and spectral intensities accurately reflected the relative site populations at 400 s.

For the experiments performed at different temperatures, although the cycle interval used (60 s) was not enough to take into account the different relative relaxation rates between silicon and silica, it allowed a comparison of the samples under equivalent conditions.

Raman Spectroscopy. A Horiba Xplora spectrometer equipped with a confocal microscope was used to collect Raman spectra. Selecting a probed area was made with a 10× objective lens and the focus of the laser beam on the sample with a 100× objective lens. The laser excitation wavelength was 633 nm and a filter to reduce the laser power to 5% of the total power was used. To separate the scattered light into its components, a 600T grating was employed. Baseline subtraction was performed on each spectrum, using a linear baseline. For each analysed sample, Raman spectra were collected in seven different spots, assessing the reproducibility of the measurements.

Notes

The authors declare no competing financial interest.

ACKNOWLEDGMENT

This project is supported by funding from the European Research Council (ERC) under the European Union's Horizon 2020 research and innovation program (Scatter, Grant agreement No. 948319). JGCV and KO recognize funding from the Natural Science and Engineering Research Council (NSERC Discovery Grant program; RGPIN-2020-04045), Alberta Innovates, the ATUMS training program supported by NSERC CREATE (CREATE-463990-2015) and the University of Alberta Faculties of Science and Graduate Studies. The France, Canada Research Fund funded travel between the University of Alberta and the University of Bordeaux. The authors acknowledge the French national project METSA for providing them with access to the microscope platform of CLYM in Lyon. *In situ* XRD measurements were performed within the ICMCB X-ray facilities. Elemental analysis was performed at the Bordeaux Imaging Center,

member of the FranceBioImaging national infrastructure (ANR-10-INBS-04). FEG-SEM observations were carried out at the Fédération de Chimie et Matériaux de Paris-Centre (FCMat FR2482), which was co-funded by Sorbonne Université, CNRS and by the C'Nano projects of the Région Ile-de-France. TEM characterization of *ex situ* heated samples were performed using facilities of the platform PLACAMAT. Anthony Chiron assisted in the heat treatment of *ex situ* samples.

ASSOCIATED CONTENT

The following files are available free of charge:

HRTEM of crystalline Si domains formed at high temperature, ETEM images showing inhomogeneous nucleation, ETEM images of a probed region showing both particle coalescence and the particle growth mode by displacement in the matrix, *in situ* XRD diffractograms collected upon HSQ heating and cooling, Table of weight loss after *ex situ* annealing under inert and reducing conditions, TEM images of *ex situ* annealed sample under inert and reducing conditions, ^{29}Si MAS NMR spectra of an *ex situ* annealed sample at different temperatures, Table of contributions of deconvoluted NMR signals, additional Raman spectra of *ex situ* annealed samples (PDF);

Video of coalescence process (.avi);

Video of particle displacement in the matrix (.avi);

Video of coalescence followed by growth by displacement in the oxide (.avi).

AUTHOR INFORMATION

Corresponding Authors

*Glenna L. Drisko. ICMCB, UMR 5026, CNRS, Univ. Bordeaux, Bordeaux INP, Pessac F-33600, France. orcid.org/0000-0001-6469-9736 ; Email: glenna.drisko@icmcb.cnrs.fr

* Cynthia Cibaka-Ndaya. ICMCB, UMR 5026, CNRS, Univ. Bordeaux, Bordeaux INP, Pessac F-33600, France. Email: cynthia.cibaka@icmcb.cnrs.fr.

*Lucian Roiban, MATEIS, UMR 5510, Univ Lyon, INSA Lyon, Université Claude Bernard Lyon 1, CNRS, 69621 Villeurbanne, France. Email : ioan-lucian.roiban@insa-lyon.fr

REFERENCES

(1) De Marco, M. L.; Semlali, S.; Korgel, B. A.; Barois, P.; Drisko, G. L.; Aymonier, C. Silicon-Based Dielectric Metamaterials: Focus on the Current Synthetic Challenges. *Angewandte Chemie International Edition* **2018**, *57* (17), 4478–4498. https://doi.org/10.1002/anie.201709044.

(2) García-Etxarri, A.; Gómez-Medina, R.; Froufe-Pérez, L. S.; López, C.; Chantada, L.; Scheffold, F.; Aizpurua, J.; Nieto-Vesperinas, M.; Sáenz, J. J. Strong Magnetic Response of Submicron Silicon Particles in the Infrared. *Opt. Express, OE* **2011**, *19* (6), 4815–4826. https://doi.org/10.1364/OE.19.004815.

(3) Kustov, P.; Petrova, E.; Nazarov, M.; Gilmullin, A.; Sandomirskii, M.; Ponkratova, E.; Yaroshenko, V.; Ageev, E.; Zuev, D. Mie-Resonant Silicon Nanoparticles for Physically Unclonable Anti-Counterfeiting Labels. *ACS Appl. Nano Mater.* **2022**, *5* (8), 10548–10559. https://doi.org/10.1021/acsanm.2c01878.

(4) Kruk, S.; Kivshar, Y. Functional Meta-Optics and Nanophotonics Governed by Mie Resonances. *ACS Photonics* **2017**, *4* (11), 2638–2649. https://doi.org/10.1021/acsphotonics.7b01038.

(5) Zograf, G. P.; Ryabov, D.; Rutckaia, V.; Voroshilov, P.; Tonkaev, P.; Permyakov, D. V.; Kivshar, Y.; Makarov, S. V. Stimulated Raman Scattering from Mie-Resonant Subwavelength Nanoparticles. *Nano Lett.* **2020**, *20* (8), 5786–5791. https://doi.org/10.1021/acs.nanolett.0c01646.

(6) Dmitriev, P. A.; Baranov, D. G.; Milichko, V. A.; Makarov, S. V.; Mukhin, I. S.; Samusev, A. K.; Krasnok, A. E.; Belov, P. A.; Kivshar, Y. S. Resonant Raman Scattering from Silicon

Nanoparticles Enhanced by Magnetic Response. *Nanoscale* **2016**, *8* (18), 9721–9726. https://doi.org/10.1039/C5NR07965A.

(7) Eslamisaray, M. A.; Wray, P. R.; Lee, Y.; Nelson, G. M.; Ilic, O.; Atwater, H. A.; Kortshagen, U. R. A Single-Step Bottom-up Approach for Synthesis of Highly Uniform Mie-Resonant Crystalline Semiconductor Particles at Visible Wavelengths. *Nano Lett.* **2023**, *23* (5), 1930–1937. https://doi.org/10.1021/acs.nanolett.2c05084.

(8) Wray, P. R.; Eslamisaray, M. A.; Nelson, G. M.; Ilic, O.; Kortshagen, U. R.; Atwater, H. A. Broadband, Angle- and Polarization-Invariant Antireflective and Absorbing Films by a Scalable Synthesis of Monodisperse Silicon Nanoparticles. *ACS Appl. Mater. Interfaces* **2022**, *14* (20), 23624–23636. https://doi.org/10.1021/acsami.2c03263.

(9) Hessel, C. M.; Henderson, E. J.; Veinot, J. G. C. Hydrogen Silsesquioxane: A Molecular Precursor for Nanocrystalline Si−SiO2 Composites and Freestanding Hydride-Surface-Terminated Silicon Nanoparticles. *Chem. Mater.* **2006**, *18* (26), 6139–6146. https://doi.org/10.1021/cm0602803.

(10) Clark, R. J.; Aghajamali, M.; Gonzalez, C. M.; Hadidi, L.; Islam, M. A.; Javadi, M.; Mobarok, M. H.; Purkait, T. K.; Robidillo, C. J. T.; Sinelnikov, R.; Thiessen, A. N.; Washington, J.; Yu, H.; Veinot, J. G. C. From Hydrogen Silsesquioxane to Functionalized Silicon Nanocrystals. *Chem. Mater.* **2017**, *29* (1), 80–89. https://doi.org/10.1021/acs.chemmater.6b02667.

(11) Milliken, S.; Thiessen, A. N.; Cheong, I. T.; O'Connor, K. M.; Li, Z.; Hooper, R. W.; Robidillo, C. J. T.; Veinot, J. G. C. "Turning the Dials": Controlling Synthesis, Structure, Composition, and Surface Chemistry to Tailor Silicon Nanoparticle Properties. *Nanoscale* **2021**, *13* (39), 16379–16404. https://doi.org/10.1039/D1NR04701A.

(12) Sugimoto, H.; Fujii, M. Colloidal Dispersion of Subquarter Micrometer Silicon Spheres for Low-Loss Antenna in Visible Regime. *Advanced Optical Materials* **2017**, *5* (17), 1700332. https://doi.org/10.1002/adom.201700332.

(13) Negoro, H.; Sugimoto, H.; Fujii, M. Helicity-Preserving Optical Metafluids. *Nano Lett.* **2023**, *23* (11), 5101–5107. https://doi.org/10.1021/acs.nanolett.3c01026.

(14) Sugimoto, H.; Okazaki, T.; Fujii, M. Mie Resonator Color Inks of Monodispersed and Perfectly Spherical Crystalline Silicon Nanoparticles. *Advanced Optical Materials* **2020**, *8* (12), 2000033. https://doi.org/10.1002/adom.202000033.

(15) Karsakova, M.; Shchedrina, N.; Karamyants, A.; Ponkratova, E.; Odintsova, G.; Zuev, D. Eco-Friendly Approach for Creation of Resonant Silicon Nanoparticle Colloids. *Langmuir* **2023**, *39* (1), 204–210. https://doi.org/10.1021/acs.langmuir.2c02382.

(16) Wang, J.; Wang, X. F.; Li, Q.; Hryciw, A.; Meldrum, A. The Microstructure of SiO Thin Films: From Nanoclusters to Nanocrystals. *Philosophical Magazine* **2007**, *87* (1), 11–27. https://doi.org/10.1080/14786430600863047.

(17) Garrido Fernandez, B.; López, M.; García, C.; Pérez-Rodríguez, A.; Morante, J. R.; Bonafos, C.; Carrada, M.; Claverie, A. Influence of Average Size and Interface Passivation on the Spectral Emission of Si Nanocrystals Embedded in SiO2. *Journal of Applied Physics* **2002**, *91* (2), 798–807. https://doi.org/10.1063/1.1423768.

(18) Choe, Han-U; U, Hyeong-Ju; 김준곤; Kim, Gi-Dong; Hong, Wan-Hong; Ji, Young-Yong. Encapsulated Silicon Nanocrystals Formed in Silica by Ion Beam Synthesis. *Bulletin of the Korean Chemical Society* **2004**, *25* (4), 525–528. https://doi.org/10.5012/BKCS.2004.25.4.525.

(19) Yang, Z.; Dobbie, A. R.; Cui, K.; Veinot, J. G. C. A Convenient Method for Preparing Alkyl-Functionalized Silicon Nanocubes. *J. Am. Chem. Soc.* **2012**, *134* (34), 13958–13961. https://doi.org/10.1021/ja3061497.
(20) Bonafos, C.; Garrido, B.; Lopez, M.; Perez-Rodriguez, A.; Morante, J. R.; Kihn, Y.; Ben Assayag, G.; Claverie, A. Ostwald Ripening of Ge Precipitates Elaborated by Ion Implantation in SiO2. *Materials Science and Engineering: B* **2000**, *69–70*, 380–385. https://doi.org/10.1016/S0921-5107(99)00411-0.
(21) Yu, D.; Lee, S.; Hwang, G. S. On the Origin of Si Nanocrystal Formation in a Si Suboxide Matrix. *Journal of Applied Physics* **2007**, *102* (8), 084309. https://doi.org/10.1063/1.2800268.
(22) Hessel, C. M.; Henderson, E. J.; Veinot, J. G. C. An Investigation of the Formation and Growth of Oxide-Embedded Silicon Nanocrystals in Hydrogen Silsesquioxane-Derived Nanocomposites. *J. Phys. Chem. C* **2007**, *111* (19), 6956–6961. https://doi.org/10.1021/jp070908c.
(23) Sato, K.; Izumi, T.; Iwase, M.; Show, Y.; Morisaki, H.; Yaguchi, T.; Kamino, T. Nucleation and Growth of Nanocrystalline Silicon Studied by TEM, XPS and ESR. *Applied Surface Science* **2003**, *216* (1), 376–381. https://doi.org/10.1016/S0169-4332(03)00445-8.
(24) Xin, Y.; Wakimoto, R.; Saitow, K. Synthesis of Size-Controlled Luminescent Si Nanocrystals from (HSiO1.5)n Polymers. *Chem. Lett.* **2017**, *46* (5), 699–702. https://doi.org/10.1246/cl.170048.
(25) Belot, V.; Corriu, R.; Leclercq, D.; Mutin, P. H.; Vioux, A. Thermal Reactivity of Hydrogenosilsesquioxane Gels. *Chem. Mater.* **1991**, *3* (1), 127–131. https://doi.org/10.1021/cm00013a029.
(26) Hartman, J. S.; Richardson, M. F.; Sherriff, B. L.; Winsborrow, B. G. Magic Angle Spinning NMR Studies of Silicon Carbide: Polytypes, Impurities, and Highly Inefficient Spin-Lattice Relaxation. *J. Am. Chem. Soc.* **1987**, *109* (20), 6059–6067. https://doi.org/10.1021/ja00254a026.
(27) Lee, D.; Kaushik, M.; Coustel, R.; Chenavier, Y.; Chanal, M.; Bardet, M.; Dubois, L.; Okuno, H.; Rochat, N.; Duclairoir, F.; Mouesca, J.; De Paëpe, G. Solid-State NMR and DFT Combined for the Surface Study of Functionalized Silicon Nanoparticles. *Chem. Eur. J.* **2015**, *21* (45), 16047–16058. https://doi.org/10.1002/chem.201502687.
(28) Pietraβ, T.; Bifone, A.; Roth, R. D.; Koch, V.-P.; Alivisatos, A. P.; Pines, A. 29Si High Resolution Solid State Nuclear Magnetic Resonance Spectroscopy of Porous Silicon. *Journal of Non-Crystalline Solids* **1996**, *202* (1), 68–76. https://doi.org/10.1016/0022-3093(96)00144-5.
(29) Shao, W.; Shinar, J.; Gerstein, B. C.; Li, F.; Lannin, J. S. Magic-Angle Spinning 29Si NMR Study of Short-Range Order in a-Si. *Phys Rev B Condens Matter* **1990**, *41* (13), 9491–9494. https://doi.org/10.1103/physrevb.41.9491.
(30) Faulkner, R. A.; DiVerdi, J. A.; Yang, Y.; Kobayashi, T.; Maciel, G. E. The Surface of Nanoparticle Silicon as Studied by Solid-State NMR. *Materials* **2013**, *6* (1), 18–46. https://doi.org/10.3390/ma6010018.
(31) Mayeri, D.; Phillips, B. L.; Augustine, M. P.; Kauzlarich, S. M. NMR Study of the Synthesis of Alkyl-Terminated Silicon Nanoparticles from the Reaction of SiCl4 with the Zintl Salt, NaSi. *Chem. Mater.* **2001**, *13* (3), 765–770. https://doi.org/10.1021/cm000418w.
(32) Caylor, R. A. Towards the Characterization of Silicon Surfaces: Solid State Nuclear Magnetic Resonance, Colorado State University, Fort Collins, Colorado, 2011.

(33) Thiessen, A. N.; Ha, M.; Hooper, R. W.; Yu, H.; Oliynyk, A. O.; Veinot, J. G. C.; Michaelis, V. K. Silicon Nanoparticles: Are They Crystalline from the Core to the Surface? *Chem. Mater.* **2019**, *31* (3), 678–688. https://doi.org/10.1021/acs.chemmater.8b03074.
(34) Richter, H.; Wang, Z. P.; Ley, L. The One Phonon Raman Spectrum in Microcrystalline Silicon. *Solid State Communications* **1981**, *39* (5), 625–629. https://doi.org/10.1016/0038-1098(81)90337-9.
(35) Harris, J. T.; Hueso, J. L.; Korgel, B. A. Hydrogenated Amorphous Silicon (a-Si:H) Colloids. *Chem. Mater.* **2010**, *22* (23), 6378–6383. https://doi.org/10.1021/cm102486w.
(36) De Marco, M. L.; Jiang, T.; Fang, J.; Lacomme, S.; Zheng, Y.; Baron, A.; Korgel, B. A.; Barois, P.; Drisko, G. L.; Aymonier, C. Broadband Forward Light Scattering by Architectural Design of Core–Shell Silicon Particles. *Advanced Functional Materials* **2021**, *31* (26), 2100915. https://doi.org/10.1002/adfm.202100915.
(37) Tsu, D. V.; Chao, B. S.; Jones, S. J. Intermediate Order in Tetrahedrally Coordinated Silicon: Evidence for Chainlike Objects. *Solar Energy Materials and Solar Cells* **2003**, *78* (1), 115–141. https://doi.org/10.1016/S0927-0248(02)00435-X.
(38) Hong, W.-E.; Ro, J.-S. Kinetics of Solid Phase Crystallization of Amorphous Silicon Analyzed by Raman Spectroscopy. *Journal of Applied Physics* **2013**, *114* (7), 073511. https://doi.org/10.1063/1.4818949.
(39) Morhange, J. F.; Kanellis, G.; Balkanski, M. Raman Study of Laser Annealed Silicon. *Solid State Communications* **1979**, *31* (11), 805–808. https://doi.org/10.1016/0038-1098(79)90392-2.
(40) Tsu, R.; Izu, M.; Ovshinsky, S. R.; Pollak, F. H. Electroreflectance and Raman Scattering Investigation of Glow-Discharge Amorphous Si:F:H. *Solid State Communications* **1980**, *36* (9), 817–822. https://doi.org/10.1016/0038-1098(80)90019-8.
(41) Anastassakis, E.; Pinczuk, A.; Burstein, E.; Pollak, F. H.; Cardona, M. Effect of Static Uniaxial Stress on the Raman Spectrum of Silicon. *Solid State Communications* **1993**, *88* (11), 1053–1058. https://doi.org/10.1016/0038-1098(93)90294-W.

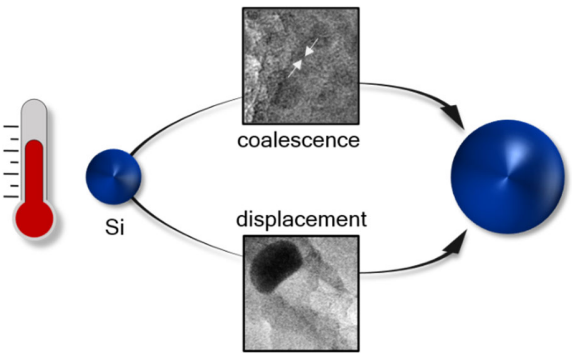

For Table of Contents only